

Inferring additional physics through unmodelled signal reconstructions

Rimo Das,^{1,2,*} V. Gayathri,^{3,†} Divyajyoti,^{4,1,2,‡} Sijil Jose,^{1,§}
Imre Bartos,⁵ Sergey Klimenko,⁵ and Chandra Kant Mishra^{1,2,¶}

¹*Department of Physics, Indian Institute of Technology Madras, Chennai 600036, India*

²*Centre for Strings, Gravitation and Cosmology, Department of Physics,
Indian Institute of Technology Madras, Chennai 600036, India*

³*Leonard E. Parker Center for Gravitation, Cosmology, and Astrophysics,
University of Wisconsin–Milwaukee, Milwaukee, WI 53201, USA*

⁴*Gravity Exploration Institute, School of Physics and Astronomy,
Cardiff University, Cardiff, CF24 3AA, United Kingdom*

⁵*Department of Physics, University of Florida, PO Box 118440, Gainesville, FL 32611-8440, USA*
(Dated: January 30, 2025)

Parameter estimation of gravitational wave data is often computationally expensive, requiring simplifying assumptions such as circularisation of binary orbits. Although, if included, the subdominant effects like orbital eccentricity may provide crucial insights into the formation channels of compact binary mergers. To address these challenges, we present a pipeline strategy leveraging minimally modelled waveform reconstruction to identify the presence of eccentricity in real time. Using injected signals, we demonstrate that ignoring eccentricity ($e_{20\text{Hz}} \gtrsim 0.1$) leads to significant biases in parameter recovery, including chirp mass estimates falling outside the 90% credible interval. Waveform reconstruction shows inconsistencies increase with eccentricity, and this behaviour is consistent for different mass ratios. Our method enables low-latency inferences of binary properties supporting targeted follow-up analyses and can be applied to identify any physical effect of measurable strength.

I. INTRODUCTION

During the second part of the third observation run (O3b) LIGO [1] and Virgo [2] detectors observed compact binary mergers with a frequency of at least one per week [3]. In the ongoing observation run (O4), detection rates have gone up by a factor of few as expected [4–6] compared to those in O3b, potentially putting significant strain on the available human and computational resources. While there have been numerous proposals in the past to help cut analysis costs, for instance, by constructing signal models that are fast to generate (see [7] for example) or by developing novel analysis methods (such as those of [8]), post-detection analyses for signals with generic features are still computationally prohibitive. As capabilities of current detectors improve (Voyager [5]), precise measurements of sub-dominant effects, such as the presence of orbital eccentricity, spin precession and higher order modes should become possible. Although, quasi-circular precessing binary black hole (BBH) mergers can be mistaken for highly eccentric mergers due to the degeneracy between the two effects [9]. Currently, a few events have been reported to be eccentric, GW190521 being one of them [10–12]. Further, inclusion of eccentricity may even become necessary for analysing data from planned

future ground-based like Cosmic Explorer (CE) [13] and Einstein Telescope (ET) [14], and space-based detectors such as DECIGO [15] and LISA [16] owing to their low-frequency sensitivity.

Parameter estimation (PE) of compact binary mergers is typically performed over a 15-dimensional parameter space comprising of intrinsic parameters such as component masses and spins and a set of extrinsic parameters including those giving location and orientation of the binary [17]. Additionally, assumptions that binary's orbits are non-circular or that its constituents are susceptible to tidal forces further extend the parameter space. However, if one can infer the absence of a specific physical effect, say for instance, of eccentricity, in that case, one can exclude it from the parameter space to be explored, thus reducing the analysis time. Conversely, observing a binary with residual orbital eccentricity in current ground-based detectors may suggest that the binary was influenced by external factors; for instance, it may have been part of a hierarchical triple system [e.g., 18], was in a densely populated star cluster [e.g., 19], or within the accretion disk of a supermassive black hole [e.g., 20–23]. Furthermore, binaries formed through dynamical interactions in dense stellar environments [24–33] or via Kozai-Lidov mechanisms [34, 35] in field triples [36, 37] could exhibit residual eccentricities of $\gtrsim 0.1$ when observed by ground-based detectors [e.g., 38–41]. However, we may miss such opportunities if eccentricity information is not included in the post-detection analyses.

In recent years, several efforts have been made to develop eccentric waveform models which may be avail-

* rimo.physics@gmail.com

† gayathri.v@ligo.org

‡ divyajyoti.physics@gmail.com

§ sijiljose.999@gmail.com

¶ ckm@iitm.ac.in

able for use in upcoming observing runs for assessing the presence of eccentricity and its impact on understanding source properties. These include several inspiral-only models for GW signals from eccentric compact binary systems, which are sufficiently accurate so that they can be compared with Numerical Relativity (NR) simulations, and are rapid enough to generate for use in direct parameter estimation via Bayesian inference [42–55]. Further, eccentric waveform models containing the inspiral, merger, and ringdown (IMR) are under development and/or are available for use [e.g., 12, 56–71], although these are typically slower to generate compared to their quasi-circular counterparts. Consequently, Bayesian inference with these models has often necessitated relaxing accuracy requirements [e.g., 72], employing likelihood reweighting methods [e.g., 73], or relying on highly resource-intensive parallel inference performed on super-computer clusters [e.g., 74, 75].

Numerous parameter estimation studies have been conducted to investigate the presence of orbital eccentricity in signals identified by standard searches optimized for quasi-circular BBH. These studies utilize available eccentric waveform models through Bayesian inference methods [e.g., 11, 12, 39, 73, 75–81] or compare the data directly with NR simulations of gravitational waves from eccentric BBH [10]. There have also been a number of studies [80, 82–91] highlighting the biases induced in parameters when eccentric signals are analysed with quasi-circular waveforms.

While the use of eccentric waveforms in template-based searches may only be realised in the future, search methods that are not sensitive to the details of the signal morphology present a suitable alternative [92–95].¹ Moreover, since the first GW detection, GW150914 [97], waveform reconstruction methods have been essential for evaluating the consistency between unmodelled reconstructions and PE results. Tools like Coherent WaveBurst [92, 93, 98, 99] (cWB) and BayesWave [100, 101] have played a key role in these efforts, with cWB providing constrained maximum-likelihood reconstructions and BayesWave utilizing the median from its posterior probability distribution. These methods have been applied extensively in GWTC catalogues [102–105] and individual event analysis, such as the detailed study of GW190521 [10, 106, 107], a rare and significant event characterized by high mass and spin-precession measurements. Tests using these methods have extracted critical physics, including higher-order modes and eccentricity. While most studies have focused on real events, the potential of waveform reconstruction for simulations remains under-explored. Leveraging these techniques in the cWB framework can serve as a powerful tool

to identify events requiring detailed follow-up, such as eccentric PE studies, motivating a deeper investigation into waveform reconstruction for eccentric systems.

The current work attempts to develop a strategy that may eventually be used to infer the presence or absence of orbital eccentricity (together with other physical effects) in observed events and, therefore, guide the offline analyses that follow the detections. Here, we target inferring the presence of orbital eccentricity in a simulated signal as a proof of principle demonstration of the method. The method, in principle, could be used to infer the presence of any additional physical effect or a superposition of sub-dominant effects that are typically ignored due to associated computational cost. The basic idea is as follows.

Let us say we have a signal present in a noisy data stream. The signal may correspond to a circular or an eccentric binary, but we do not have this information a priori. In order to infer the nature of the binary, we propose the following. First, we perform a detailed parameter estimation exercise using a circular state-of-the-art model.² Naturally, the measurements will be consistent with a circular binary even though the signal is eccentric, and our estimates may be biased. The bias may be small or large depending upon the binary’s eccentricity. In any case, the results (posterior distributions) will represent an effective measurement of source properties. If one also has an eccentric waveform that can be used for PE, one could simply repeat the exercise and obtain an unbiased estimation of parameters together with a measurement of the binary’s orbital eccentricity. But let’s assume we do not have such a model, or even if we do, using it for a detailed analysis is computationally expensive. In such situations, we propose that search methods developed within the cWB framework on data may be employed. The output is a reconstructed signal that is expected to capture all relevant physics of the signal. One may then plan to reconstruct signals based on posterior distributions of the PE analysis and compare with the one obtained using direct reconstruction above. The expectation is that if the signal is circular, the two reconstructions will match. Hence, any significant loss of match will indicate the presence of eccentricity in the system and thus provide an indirect inference of the same. This methodology can be extended to other effects which may modify the gravitational wave signal such as compact binaries in the presence of astrophysical environments [109, 110], mergers of boson star binaries [111, 112], etc. but are not currently accounted for in the standard PE exercises. Figure 1 displays the detailed methodology.

Our investigations involve injecting a set of eccentric

¹ No evidence for the presence of eccentricity was found using these methods in the data for the first two observing runs [75, 96].

² In practice, we may simply use the results of any online PE analysis[108] so as to perform the exercise with low latency.

IMR signals both for PE and waveform reconstruction studies. These were obtained from hybrids constructed by combining post-Newtonian (PN) waveforms and NR simulations in an earlier work [61]. This paper is organised as follows. Section II summarises the methodology adopted for quantifying the detection of an eccentric GW mode. Waveforms, detector configuration and other necessary inputs are also included in this section. Section III presents our findings. Finally, Sec. IV includes a comprehensive summary of our findings and future directions.

II. METHODOLOGY

A. Simulations

The full inspiral-merger-ringdown hybrids are constructed by matching the PN waveforms and NR simulations. The matching is performed in a region where the PN prescription matches the NR data by more than 99% following the method in Ref [113]. The PN expressions of GW modes for the inspiral part, which are 3PN accurate in amplitude [45, 49, 50] and 3.5PN accurate in phase [47, 114], assuming non-spinning compact objects in quasi-elliptical orbits, are computed based on Quasi-Keplerian representation in Refs [115–117]. The NR simulations, which model the late inspiral and merger-ringdown phases to capture strong-field gravity effects, have been performed using the Spectral Einstein Code (SpEC) developed by the SXS Collaboration [118, 119]. In our study, we considered only ($l = 2$, $|m| = 2$) or simply 22 mode for the hybrid signal. The effects of subdominant modes such as ($l, |m|$) = (3, 3), (4, 4), (5, 5), (2, 1), (3, 2), and (4, 3) have not been used in this analysis. The reason for taking only the dominant mode is that any additional systematics other than eccentricity can bias the parameter estimation study, affecting our further cWB analysis. In our analyses, we have used twenty-one non-spinning eccentric hybrids from Ref [61] with mass ratios ($q = 1, 2, 3$) and initial eccentricities ($e_{15.4} \leq 0.36$). The eccentricity at 20 Hz has been calculated by using the equation 4.17 in Ref [46]. These simulated signals act as a proxy for the actual GW signal in the detector. The details of the hybrids are mentioned in TABLE I of Ref [61].

B. CWB reconstructions

Coherent WaveBurst (cWB) [92, 94, 98, 99], a model-independent search pipeline has been used by the LIGO-Virgo-Kagra (LVK) Collaboration to both detect and reconstruct gravitational waveforms without assumptions about the source. cWB uses wavelet transformation to convert detector data into a time-frequency representation and identifies potential candidates by clustering time-frequency pixels with higher coherent energy. These

clusters undergo a series of noise veto checks, with surviving candidates considered gravitational-wave events.

For each event, cWB computes summary statistics describing properties such as signal duration, central frequency, and correlation across detectors. Thresholds are applied to these statistics to distinguish true GW events from noise fluctuations, improving the significance of candidate events.

A key feature of cWB is its ability to reconstruct waveforms for detected candidates through inverse wavelet transformation, a process that makes minimal assumptions about the signal shape and is often referred to as minimal modelling. By comparing these reconstructed waveforms with those obtained through PE using quasi-circular templates, we can identify unexpected behaviours in GW events that are not captured by traditional PE models. Although no comprehensive eccentric waveform template bank currently exists, cWB’s model-independent approach allows it to maintain sensitivity to eccentric mergers, making it a powerful tool for studying eccentric systems.

C. Figures of merit: overlap distribution

A waveform consistency test has been developed to quantify this discrepancy [10, 107]. This test involves performing a series of dedicated CBC injections with the samples derived from the posterior distributions of the source parameters. In this test, randomized samples are injected (extracted from PE analysis of the event) into the GW data near the event times. Then, we run the cWB waveform reconstruction algorithm on this data. These randomly injected samples are referred to as “null-sources” injections, while the waveform reconstructed from the actual event data is known as “on-source”. At the end of the cWB analysis, we have waveform reconstruction for each injection.

The waveform match or overlap is defined as,

$$\mathcal{O}(h_1, h_2) = \frac{\langle h_1 | h_2 \rangle}{\sqrt{\langle h_1 | h_1 \rangle \langle h_2 | h_2 \rangle}} \quad (1)$$

where h_1 and h_2 are the two written waveforms, and $\langle | \rangle$ represents the noise-weighted inner product. An overlap value of 1 indicates a perfect overlap between waveforms, while a value close to 0 indicates that the correlation between waveforms is nil.

Let us assume that W_i represents the cWB point waveform reconstruction estimate of h_i . The waveform $W = W_k(t)$ is estimated through a model-independent point estimate and a selected whitened waveform from a given signal model $h = h_k(t)$, where k represents detector index. We estimate an overlap between the off-source injection (h_i) and its cWB waveform reconstruction (W_i), which we consider as the null-distribution $\mathcal{O}_o(W_i, h_i)$, where index i represents injection. This null distribution reveals a mismatch caused by both the cWB waveform reconstruction and noise. Additionally, we compute

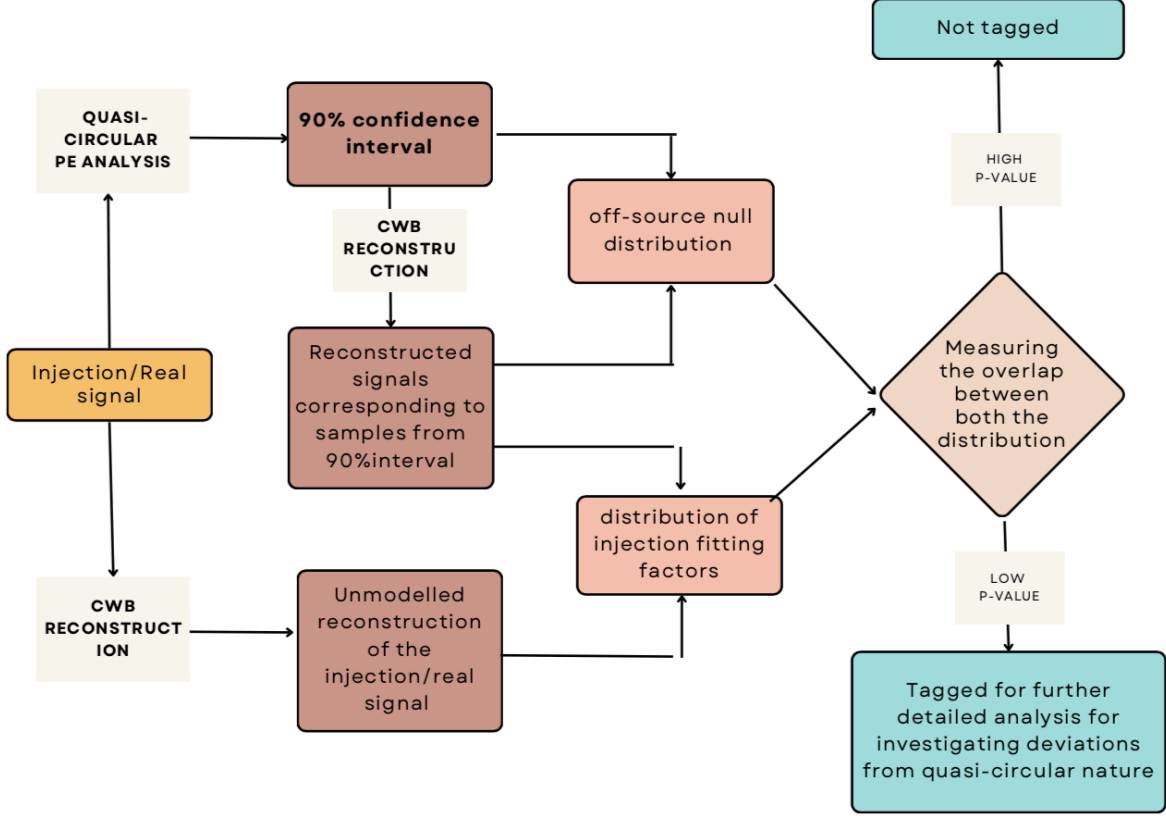


FIG. 1: A flow chart describing the methodology used in this paper. The injected signal is reconstructed using cWB (lower brown block) and signals corresponding to the PE samples within 90% credible interval (upper brown block) are reconstructed again using cWB (middle brown block). Null distribution is obtained by calculating overlap of PE samples with corresponding reconstructions. Subsequently, the injection fitting factor distribution is obtained using overlap between the reconstruction of injected waveform and reconstructions corresponding to PE samples. The deviation between the two distributions is characterised by the p-value. Low p-value events can be tagged for further detailed analysis with different waveform approximants.

the on-source overlap distribution denoted as $\mathcal{O}(W, h_p)$, where p denotes a proxy signal and W is a reconstruction of the event.

The on-source overlap, denoted as \mathcal{O} , is calculated using the point waveform reconstruction W for the GW event and h_p as a proxy for the true GW signal, selected from the posterior distribution. If the model accurately describes the GW event, we anticipate that the overlap $\mathcal{O}(W, h_p)$ will fall within the null distribution. If the observed signal W contains additional information, such as eccentricity, that is not accounted for by the waveform model used for PE, the on-source overlap \mathcal{O} will decrease and deviate from the null distribution. These deviations give a hint of the presence of eccentricity, which we can use to sub-select interesting GW candidates.

We define the equation for the figure of merit as follows,

$$\Delta_{median} = M_1 - M_2 \quad (2)$$

where M_1 and M_2 are the medians of null and on-source distribution respectively.

III. RESULTS

A. Parameter estimation

In this section, we perform injection studies using the eccentric hybrids constructed in Chattaraj et al. [61] to assess the biases that are introduced when quasi-circular waveforms are used to recover eccentric signals. The complete information of the hybrids used for injections is given in Table I in [61]. We inject the signals in Gaussian noise simulated from the power spectral density of the detectors and use the inspiral-merger-ringdown waveform model IMRPHENOMXAS [120] for recovery. We employ Bayesian inference to compute the likelihood and, hence,

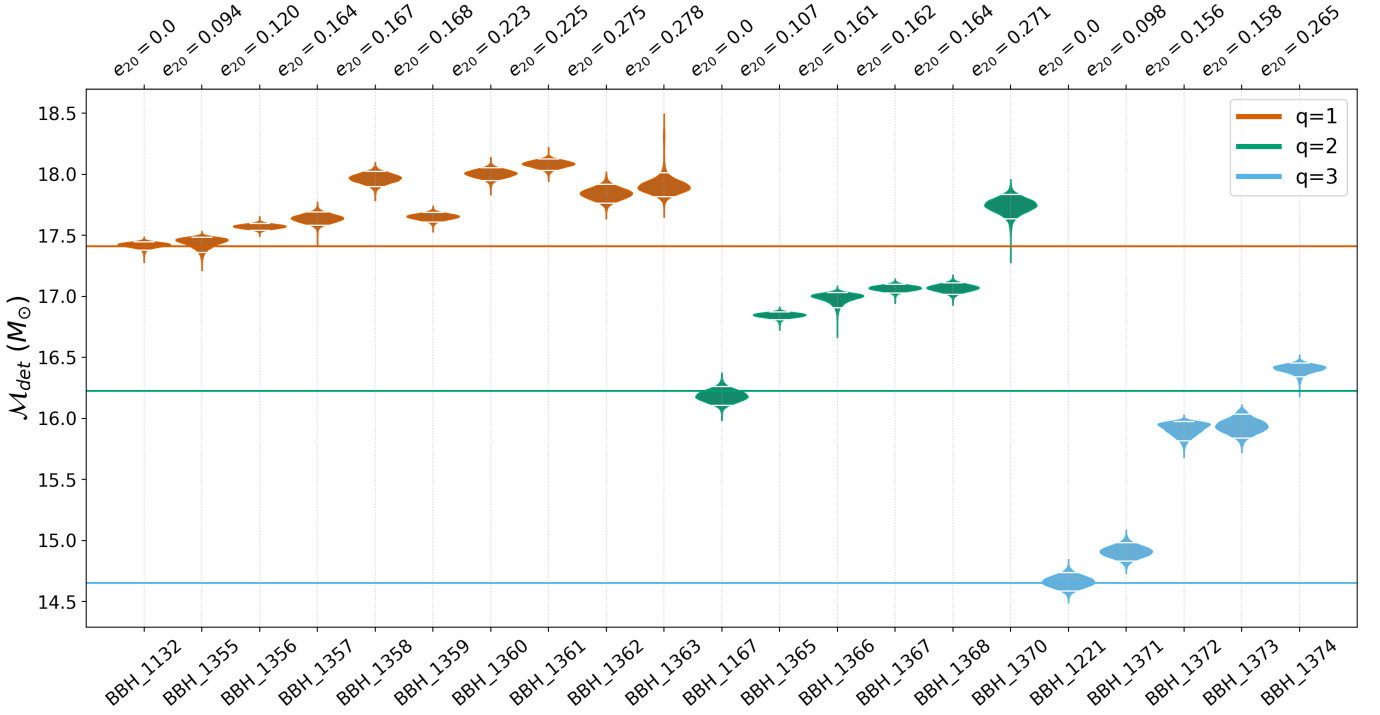


FIG. 2: Violin plots showing the chirp mass posteriors for various hybrids. The horizontal axis shows the hybrid ID and corresponding eccentricity at 20 Hz at the bottom and the top respectively. Different colours correspond to different mass ratios with the coloured horizontal lines denoting the injected values of chirp mass for the respective mass ratios. The small horizontal white lines inside the violins denote the 90% credible interval. It can be seen that the posteriors for hybrids with low eccentricities include the injected values whereas as the eccentricity is increased, the chirp mass posteriors become biased. The matched filter SNRs lie in the range of $\sim 29 - 45$ depending on the mass ratio and eccentricity values of the system.

construct the posteriors. We assume that our sources are at a distance of 410 Mpc and inclined at an arbitrary angle of 30° to the line of sight. We have fixed the total mass to $40 M_\odot$ and the mass ratio varies as [1,2,3] depending on the hybrid (see Table I in [61]). The right-ascension (α), declination (δ), and polarization (ψ) angles are chosen arbitrarily with the values 30° , 45° , and 60° respectively, and the geocent time (t_{gps}) is taken to be 1137283217 s. Since the signal-to-noise ratio (SNR) of a GW signal depends not only on intrinsic parameters, such as mass and eccentricity but also on extrinsic parameters, variation in these parameters can result in different SNRs, thereby affecting the widths of the posteriors presented in this analysis.

The Bayesian posterior probability for a parameter $\vec{\theta}$, given the data \vec{s} and a GW model \mathcal{H} , is given by

$$p(\vec{\theta}|\vec{s}, \mathcal{H}) = \frac{\mathcal{L}(\vec{s}|\vec{\theta}, \mathcal{H})\pi(\vec{\theta}, \mathcal{H})}{\mathcal{Z}(\vec{s})}, \quad (3)$$

where $\mathcal{L}(\vec{s}|\vec{\theta}, \mathcal{H})$ represents the likelihood, $\pi(\vec{\theta}, \mathcal{H})$ is the prior, and $\mathcal{Z}(\vec{s}|\mathcal{H})$ represents the evidence. We use PyCBC [121] to create injections, LALSimulation [122] for generating waveforms, and the *nested* sampling algorithm [123] implemented through *dynesty* [124] sam-

pler in *bilby* [125] and *bilby_pipe* [126] for parameter estimation.

All injections are non-spinning, so the component spin vectors have been set to zero during recovery. We sample the parameter space that includes chirp mass (\mathcal{M}), inverse mass ratio ($q_{\text{inv}} = m_2/m_1$), geocentric time (t_c), luminosity distance (d_L), phase angle (ϕ_c), inclination angle (θ_{in}), right ascension (α), declination (δ), and polarization angle (ψ). The complete information on priors is presented in Appendix A. In the following subsections, we use the term “recovery” to describe a result where the injected value falls within the 90% credible interval of the posterior, and the systematic bias (defined as the difference between the median value and the injected value) is smaller than the posterior’s width at 90% confidence. We consider a result to exhibit significant bias if the injected value lies entirely outside the 90% credible interval of the posterior. As noted earlier, these biases depend on the SNRs, which in this study are within the range of typical SNRs observed in gravitational wave event catalogues. We use the LHV network with design sensitivities of Advanced LIGO [127] for LIGO-Hanford and LIGO-Livingston, and design sensitivity of Virgo [128] detectors to perform all the parameter estimation analyses shown here.

We present the results for parameter estimation in Fig. 2. Here we plot the chirp mass posteriors for all the hybrids in the form of violin plots. The bottom and top axes of the plot label the simulation ID and the eccentricity value at 20 Hz for the corresponding hybrids, respectively. The colours orange, green, and blue correspond to mass ratios 1, 2, and 3, respectively, with the injected chirp mass values shown as the same colour horizontal lines on the plot. Small white lines inside the filled curve denote 90% credible interval for each violin.

It can be seen that the injected values of chirp mass lie within the 90% credible intervals for simulations with low values of eccentricity such as BBH_1132, BBH_1355, BBH_1167, and BBH_1221 but as we go to hybrids with higher eccentricities, the posteriors become increasingly biased. Since an eccentric signal is shorter in length than its circular counterpart, when eccentric injections are analysed using quasi-circular waveforms, higher mass templates are picked up to compensate for the shorter signals. Hence we see a bias towards higher chirp mass as the value of eccentricity is increased. For hybrids with the same mass ratio and with similar values of eccentricity (e.g. BBH_1358 and BBH_1359), a difference in the mean anomaly (see Table I in [61]) can result in different biases. In the following sections, we highlight how these biases result in various differences in the reconstructed waveforms and hence help us identify the signature of eccentricity with cWB.

B. cWB Waveform Reconstruction

1. Reconstructed Waveforms

We perform the cWB-waveform reconstructions for all injections mentioned in the PE section. The details about cWB reconstruction are discussed in Section II B. These analyses were performed in Gaussian noise with Advanced LIGO and Virgo sensitivity.

Fig 3 shows the reconstructed whitened strain for parameter estimation of select hybrids. The orange curve represents the reconstructed whitened waveform for a hybrid injection by cWB for the LIGO Livingston detector. The light gray shaded regions denote the 90% credible intervals derived from the waveform reconstruction of the PE samples, and the black curve corresponds to the median of these reconstructed waveforms. The top, middle and bottom rows represent results from selected hybrids with $q = 1, 2$ & 3 , respectively. The left and right columns refer to zero and maximum eccentricity hybrid injection, respectively, for a given mass ratio. It is well understood that eccentricity influences the signal duration; for a fixed-mass binary, the signal duration decreases as eccentricity increases. This trend is observable in Fig 3, moving from left to right.

We observe that for hybrids with no eccentricity (left column of Fig. 3), the reconstructed signal lies within the 90% credible interval (shaded gray region). However,

for eccentric hybrid injections (right column of Fig. 3), discrepancies arise between the 90% reconstruction band and the injected reconstruction. These discrepancies become more pronounced as eccentricity increases and are observed in both the time and frequency domains. For hybrids with higher eccentricity (e.g., BBH_1361, BBH_1363), the reconstructed strain not only falls significantly outside the gray region but also shows a considerable phase deviation from the median of the PE samples.

2. Figures of Merit: Overlap Distribution

In this section, we present the results of the figure-of-merit analysis conducted for the injected signals. Overlap factors were computed using Equation (1) for all simulated signals, following the methodology outlined in the flow chart. Fig. 4 illustrates the overlap distributions for on-source (orange) and null (blue) cases across various cWB reconstruction analyses for $q = 1$. The vertical dashed lines denote the median for on-source and null distributions respectively.

Subplot (a) corresponds to zero eccentricity, while subplots (b), (c), (d), (e), and (f) depict analyses of injections with eccentricity arranged in increasing order. The null distribution compares the overlap between the injected PE sample waveform and its cWB waveform reconstruction. In contrast, the on-source distribution compares the cWB reconstruction of the hybrid injection to the PE sample cWB waveform reconstruction.

We observe that the null histogram exhibits a relatively consistent distribution of overlap values across different cases. However, this behaviour changes for high eccentricity ($e_{20} = 0.278$) case, most likely due to a loss in low-energy pixels during the reconstruction process. Significant deviations in the overlap between the two histograms can be identified with increasing eccentricity. Specifically, the overlap refers to the common region enclosed by the two histograms within their 90% area about the median. Beyond a certain eccentricity threshold, the overlap diminishes to nearly zero, indicating a substantial difference between the PE sample cWB waveform reconstruction and the hybrid injection reconstruction.

To quantify this behaviour, we introduce a new metric that measures the difference between the medians of the two histograms (Eq. 2) as a function of eccentricity. This metric provides a clearer indication of how waveform reconstruction consistency degrades with increasing eccentricity. We present a figure of merit Fig. 5 for different hybrids. Each data point in the scatter plot corresponds to a specific eccentricity and mass ratio, capturing trends and variations across these parameters. As eccentricity increases, the value of Δ_{median} increases, indicating that the eccentricity feature is observable in Δ_{median} . This trend remains consistent across different mass ratios. We have plotted the figure of merit with error bars where, errors in the median shift are calculated using standard error propagation method. For $q = 1, 2$ and 3 ,

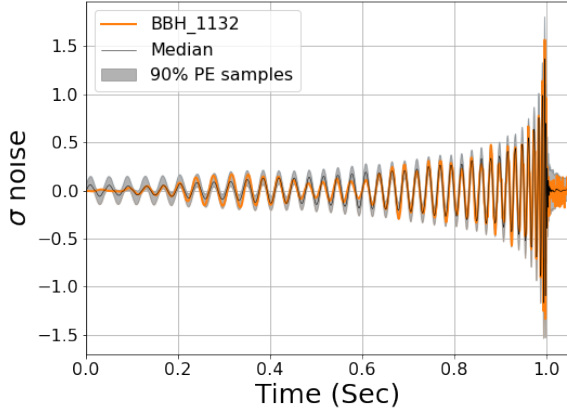
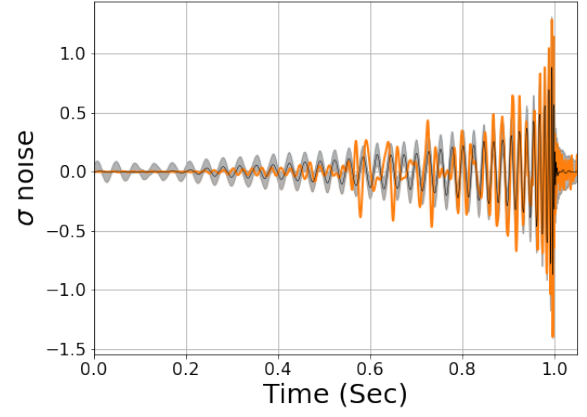
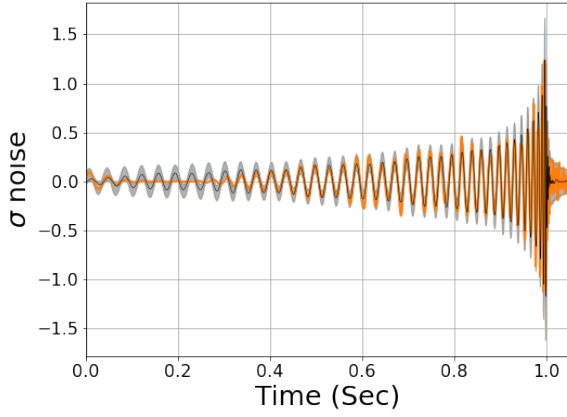
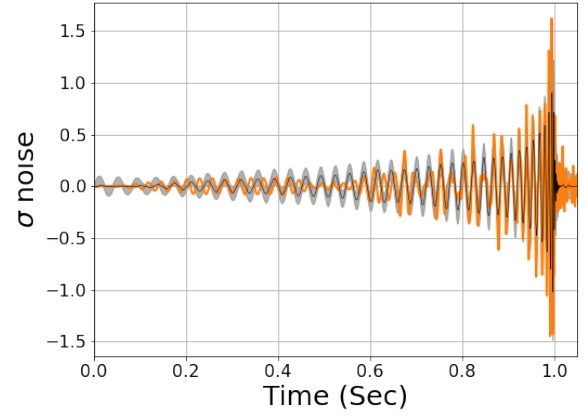
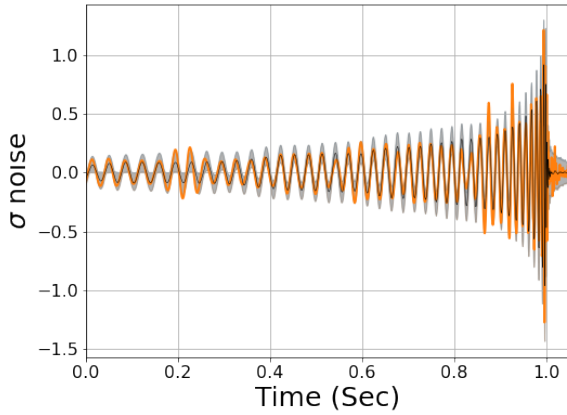
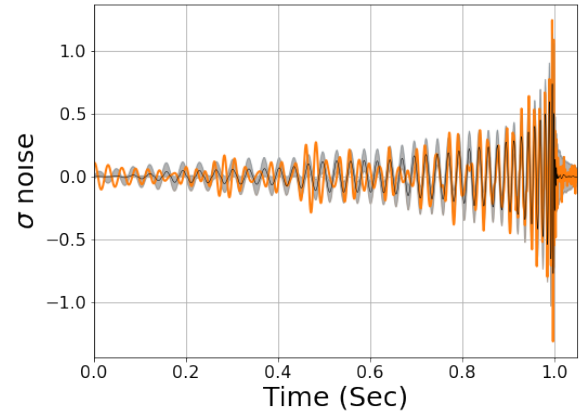
(a) BBH 1132: $q = 1$ and zero-eccentricity(b) BBH 1363: $q = 1$ and $e_{20} = 0.278$ (c) BBH 1167: $q = 2$ and zero-eccentricity(d) BBH 1370: $q = 2$ and $e_{20} = 0.271$ (e) BBH 1221: $q = 3$ and zero-eccentricity(f) BBH 1374: $q = 3$ and $e_{20} = 0.265$

FIG. 3: Reconstructed whitened strain using cWB for a given parameter estimation run. The orange curve represents the whitened waveform of the hybrid injection as reconstructed by cWB for the LIGO Livingston detector. The light gray shaded regions denote the 90% credible intervals derived from the waveform reconstruction of the PE samples. The top, middle, and bottom rows represent results from hybrid analysis for $q = 1, 2$ & 3 , respectively. The left and right columns denote zero and non-zero eccentricity, respectively.

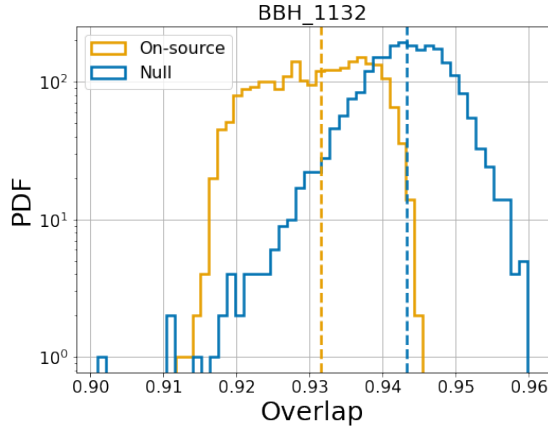
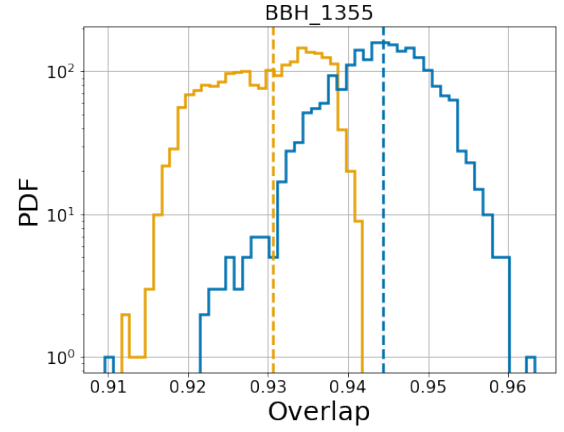
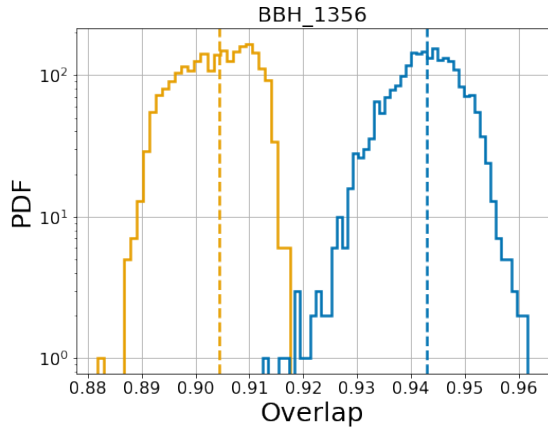
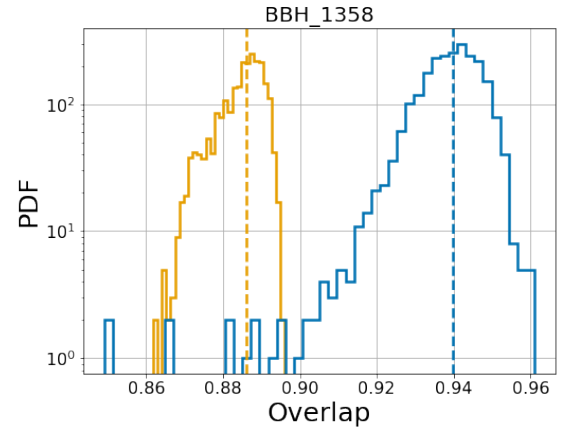
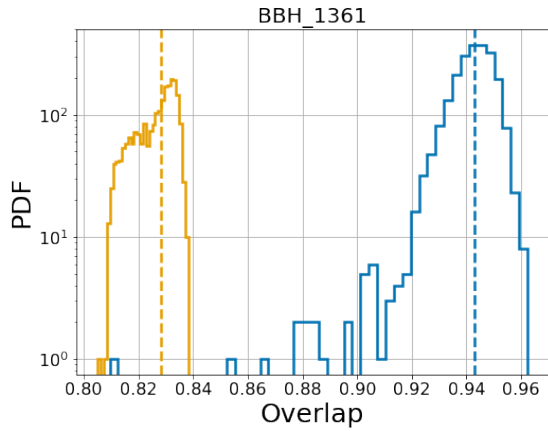
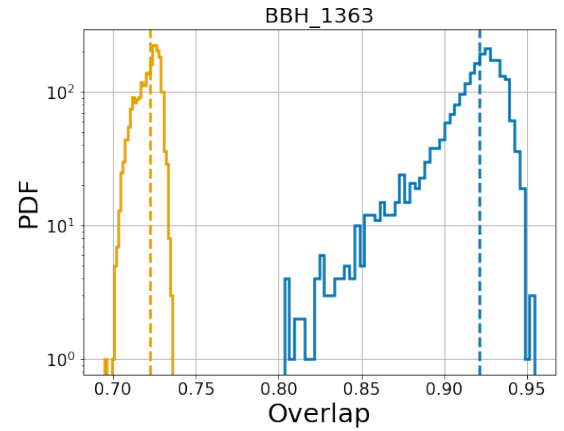
(a) BBH 1132: $q = 1$ and zero-eccentricity(b) BBH 1355: $q = 1$ and $e_{20} = 0.094$ (c) BBH 1356: $q = 1$ and $e_{20} = 0.120$ (d) BBH 1358: $q = 1$ and $e_{20} = 0.167$ (e) BBH 1361: $q = 1$ and $e_{20} = 0.225$ (f) BBH 1363: $q = 1$ and $e_{20} = 0.278$

FIG. 4: Overlap histograms showing on-source (orange) and null (blue) distributions for different cWB reconstruction analyses with $q = 1$. The dashed orange and blue lines represent medians for on-source and null distributions, respectively. Subplot (a) corresponds to zero eccentricity, while subplots (b), (c), (d), (e), and (f) represent analyses of injections with increasing eccentricity values.

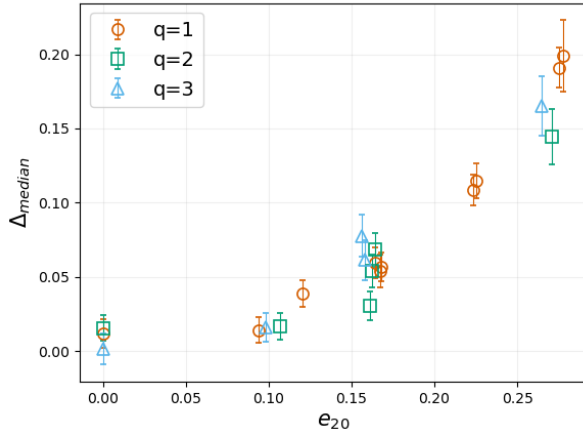


FIG. 5: Plot of Δ_{median} for different values of eccentricity. Each color corresponds to a specific mass ratio, illustrating the variation across events.

the maximum errors in the median shift corresponding to the highest eccentricity are 0.024, 0.018 and 0.020 respectively. We have also calculated the relative shifts in Δ_{median} for eccentric injections with respect to the circular one. The values for the relative shifts are 15.9, 8.45 and 137.17 corresponding to highest eccentricity for $q = 1, 2$ and 3 respectively. These deviations represent the combined contributions of biases in CBC parameter estimation and effects from cWB waveform reconstruction. It is important to note that this analysis was conducted in Gaussian noise; for real noise scenarios, these results will be influenced by noise fluctuations.

IV. CONCLUSION AND FUTURE DIRECTIONS

In this section, we summarize our results from the above analysis. The motivation to hunt for eccentric binary mergers is to gain information about the formation channel of the binaries. A binary formed in dense stellar environment or in a three-body interaction can have residual eccentricity $e_{20} \gtrsim 0.1$ which is likely to be detected in the ground-based detectors. Hence, ignoring eccentricity in the waveform model can result in a loss of SNR in a matched filter search. However, computational expenses continue to increase exponentially in parameter estimation studies with added parameters. Therefore, we explore the detectability of eccentricity using unmodelled waveform reconstruction algorithm.

Our results can be divided into two parts: parameter estimation analysis and waveform reconstruction study (see Fig. 1 for a flow chart describing the methodology). We inject hybrid signals of total mass $40M_{\odot}$ into Gaussian noise and perform PE using a quasi-circular

waveform model, IMRPHENOMXAS [120]. The violin plot in Fig. 2 shows the effect of ignoring eccentricity greater than 0.1 at 20Hz (e_{20}) for $q = (1, 2, 3)$ as the recovered chirp mass is outside the 90% credible interval. Similar biases are also noticed in recovering other intrinsic parameters such as total mass and mass ratio with increasing eccentricity. Additionally, in the waveform reconstruction analysis (see Fig. 3) we observe that for $e_{20} \gtrsim 0.1$ the reconstructed waveform is inconsistent with the 90% credible interval and is out of phase. We compute the overlap factor for on-source and null distributions discussed in section II C. For the on-source analysis, we find that with increasing eccentricity, the overlap factor reduces sharply and reaches $\sim 75\%$ for $e_{20} \simeq 0.27$. As a result, the on-source distribution deviates from the null distribution, which is also evident from Fig. 5. Thus, we can conclude that the orbital eccentricity of a binary system, which is a sub-dominant effect, can be isolated even in cases where eccentric waveforms are not readily accessible. The methodology is so robust that it can be employed to infer the presence of any sub-dominant physical effect, such as the presence of precession effects in the signal due to spin and/or higher-order modes apart from eccentricity. In future work, we plan to extend the methods presented here to analyse real events, which, in principle, can include a combination of these sub-dominant effects.

Overall, our results demonstrate that eccentricity introduces measurable inconsistencies in waveform reconstruction. These findings emphasize the necessity for incorporating eccentricity into waveform models and analysis pipelines to enhance reconstruction accuracy for gravitational wave signals.

ACKNOWLEDGMENTS

We thank Juan Calderón Bustillo for his useful comments on the manuscript. RD thanks the Gravitation and Cosmology Group at IIT Madras for numerous insightful discussions. RD also thanks Tanmaya Mishra for helping fix a few issues with the cWB pipeline installation. DJ acknowledges the Science and Technology Facilities Council (STFC) for support through grants ST/V005618/1 and ST/Y004272/1. G.V. acknowledges the support of NSF under grant PHY-2207728. S.K. acknowledges the support of NSF under grants PHY 2110060 and PHY-2409372. I.B acknowledges the support of NSF under grants PHY-2309024. C.K.M. acknowledges the support of SERB's Core Research Grant No. CRG/2022/007959. Computations were performed on CIT, LHO, and LLO clusters provided by the LIGO Laboratory and supported by the National Science Foundation Grants PHY-0757058 and PHY-0823459. This material is based upon work supported by NSF's LIGO Laboratory, which is a major facility fully funded by the National Science Foundation.

We used the following software packages: LALSuite [122], bilby [125], bilby_pipe [126], PyCBC [129], NumPy [130], PESummary [131], Matplotlib [132], Seaborn [133], jupyter [134], and dynesty [124]. This document has LIGO preprint No. LIGO-P2400590.

Appendix A: Priors used for parameter estimation

The sample space for parameter estimation includes the following parameters: inverse mass ratio ($q_{\text{inv}} = m_2/m_1$),³ chirp mass (\mathcal{M}), luminosity distance (d_L), inclination angle (θ_{jn}), geocentric time (t_c), phase angle (ϕ_c), right ascension (α), declination (δ), and polarization angle (ψ). We have put constraint on component masses as $[5, 50]M_\odot$. The priors for all the parameters are given in Table I.

Parameter	Prior	Range
\mathcal{M}	Uniform	5 - $50M_\odot$
q_{inv}	Uniform	0.125 - 1
d_L	Uniform Source Frame	100 - 1000 Mpc
θ_{jn}	Uniform sine	0 - π
ϕ_c	Uniform	0 - 2π
α	Uniform	0 - 2π
δ	Uniform cos	$-\pi/2$ - $\pi/2$
ψ	Uniform	0 - π
t_c	Uniform	$t_{\text{gps}} \pm 0.1$ s

TABLE I: Priors for parameters used in precessing spin recoveries.

-
- [1] J. Aasi *et al.* (LIGO Scientific), *Class. Quant. Grav.* **32**, 074001 (2015), arXiv:1411.4547 [gr-qc].
- [2] F. Acernese *et al.* (VIRGO), *Class. Quant. Grav.* **32**, 024001 (2015), arXiv:1408.3978 [gr-qc].
- [3] R. Abbott *et al.* (LIGO Scientific, VIRGO, KAGRA), arXiv preprint (2021), arXiv:2111.03606 [gr-qc].
- [4] D. Shoemaker (LIGO Scientific), (2019), arXiv:1904.03187 [gr-qc].
- [5] LIGO Scientific Collaboration, (2016).
- [6] B. P. Abbott *et al.* (KAGRA, LIGO Scientific, Virgo, VIRGO), *Living Rev. Rel.* **21**, 3 (2018), arXiv:1304.0670 [gr-qc].
- [7] M. Pürrer, *Class. Quant. Grav.* **31**, 195010 (2014), arXiv:1402.4146 [gr-qc].
- [8] R. Smith, S. E. Field, K. Blackburn, C.-J. Haster, M. Pürrer, V. Raymond, and P. Schmidt, *Phys. Rev. D* **94**, 044031 (2016), arXiv:1604.08253 [gr-qc].
- [9] J. Calderón Bustillo, N. Sanchis-Gual, A. Torres-Forné, and J. A. Font, *Phys. Rev. Lett.* **126**, 201101 (2021), arXiv:2009.01066 [gr-qc].
- [10] V. Gayathri, J. Healy, J. Lange, B. O’Brien, M. Szczepanczyk, I. Bartos, M. Campanelli, S. Klimenko, C. O. Lousto, and R. O’Shaughnessy, *Nature Astron.* **6**, 344 (2022), arXiv:2009.05461 [astro-ph.HE].
- [11] I. M. Romero-Shaw, P. D. Lasky, E. Thrane, and J. C. Bustillo, *Astrophys. J. Lett.* **903**, L5 (2020), arXiv:2009.04771 [astro-ph.HE].
- [12] H. L. Iglesias *et al.*, (2022), arXiv:2208.01766 [gr-qc].
- [13] S. Dwyer, D. Sigg, S. W. Ballmer, L. Barsotti, N. Mavalvala, and M. Evans, *Phys. Rev. D* **91**, 082001 (2015), arXiv:1410.0612 [astro-ph.IM].
- [14] M. Punturo *et al.*, *Class. Quant. Grav.* **27**, 194002 (2010).
- [15] S. Sato *et al.*, *Journal of Physics: Conference Series* **840**, 012010 (2017).
- [16] P. Amaro-Seoane, H. Audley, S. Babak, *et al.*, arXiv e-prints, arXiv:1702.00786 (2017), arXiv:1702.00786 [astro-ph.IM].
- [17] B. P. Abbott *et al.* (LIGO Scientific, Virgo), *Phys. Rev. Lett.* **116**, 241102 (2016), arXiv:1602.03840 [gr-qc].
- [18] F. Antonini, S. Toonen, and A. S. Hamers, *ApJ* **841**, 77 (2017), arXiv:1703.06614 [astro-ph.GA].
- [19] C. L. Rodriguez, P. Amaro-Seoane, S. Chatterjee, and F. A. Rasio, *Phys. Rev. Lett.* **120**, 151101 (2018), arXiv:1712.04937 [astro-ph.HE].
- [20] H. Tagawa, B. Kocsis, Z. Haiman, I. Bartos, K. Omukai, and J. Samsing, *ApJ* **907**, L20 (2021), arXiv:2010.10526 [astro-ph.HE].
- [21] I. Bartos, B. Kocsis, Z. Haiman, and S. Márka, *Astrophys. J.* **835**, 165 (2017), arXiv:1602.03831 [astro-ph.HE].
- [22] Y. Yang, V. Gayathri, I. Bartos, Z. Haiman, M. Safarzadeh, and H. Tagawa, *Astrophys. J. Lett.* **901**, L34 (2020), arXiv:2007.04781 [astro-ph.HE].
- [23] V. Gayathri, Y. Yang, H. Tagawa, Z. Haiman, and I. Bartos, *Astrophys. J. Lett.* **920**, L42 (2021), arXiv:2104.10253 [gr-qc].
- [24] S. F. Portegies Zwart and S. McMillan, *Astrophys. J. Lett.* **528**, L17 (2000), arXiv:astro-ph/9910061.
- [25] J. M. B. Downing, M. J. Benacquista, M. Giersz, and R. Spurzem, *MNRAS* **407**, 1946 (2010), arXiv:0910.0546 [astro-ph.SR].
- [26] C. L. Rodriguez, S. Chatterjee, and F. A. Rasio, *Phys. Rev. D* **93**, 084029 (2016), arXiv:1602.02444 [astro-ph.HE].
- [27] S. Banerjee, *Mon. Not. Roy. Astron. Soc.* **473**, 909 (2018), arXiv:1707.00922 [astro-ph.HE].
- [28] U. N. Di Carlo, N. Giacobbo, M. Mapelli, M. Pasquato, M. Spera, L. Wang, and F. Haardt, *Mon. Not. Roy. Astron. Soc.* **487**, 2947 (2019), arXiv:1901.00863 [astro-ph.HE].
- [29] M. Mapelli, “Formation channels of single and binary stellar-mass black holes,” in *Handbook of Gravitational Wave Astronomy*, edited by C. Bambi, S. Katsanevas, and K. D. Kokkotas (Springer Singapore, Singapore,

³ We use the word *inverse* here to indicate that this is inverse of the *mass ratio* we have used throughout the paper. Please note that bilby uses the term `mass_ratio` for this.

- 2020) pp. 1–65.
- [30] I. Mandel and A. Farmer, *Phys. Rept.* **955**, 1 (2022), [arXiv:1806.05820 \[astro-ph.HE\]](#).
 - [31] J. Samsing, *Phys. Rev. D* **97**, 103014 (2018), [arXiv:1711.07452 \[astro-ph.HE\]](#).
 - [32] G. Fragione, E. Grishin, N. W. C. Leigh, H. B. Perets, and R. Perna, *Mon. Not. Roy. Astron. Soc.* **488**, 47 (2019), [arXiv:1811.10627 \[astro-ph.GA\]](#).
 - [33] J. Samsing, I. Bartos, D. J. D’Orazio, Z. Haiman, B. Kocsis, N. W. C. Leigh, B. Liu, M. E. Pessah, and H. Tagawa, *Nature* **603**, 237 (2022), [arXiv:2010.09765 \[astro-ph.HE\]](#).
 - [34] Y. Kozai, *Astron. J.* **67**, 591 (1962).
 - [35] M. Lidov, *Planetary and Space Science* **9**, 719 (1962).
 - [36] M. A. S. Martinez *et al.*, *Astrophys. J.* **903**, 67 (2020), [arXiv:2009.08468 \[astro-ph.GA\]](#).
 - [37] S. Naoz, *ARA&A* **54**, 441 (2016), [arXiv:1601.07175 \[astro-ph.EP\]](#).
 - [38] I. Kowalska, T. Bulik, K. Belczynski, M. Dominik, and D. Gondek-Rosinska, *A&A* **527**, A70 (2011), [arXiv:1010.0511 \[astro-ph.CO\]](#).
 - [39] M. E. Lower, E. Thrane, P. D. Lasky, and R. Smith, *Phys. Rev. D* **98**, 083028 (2018), [arXiv:1806.05350 \[astro-ph.HE\]](#).
 - [40] J. Samsing and E. Ramirez-Ruiz, *Astrophys. J. Lett.* **840**, L14 (2017), [arXiv:1703.09703 \[astro-ph.HE\]](#).
 - [41] M. Zevin, I. M. Romero-Shaw, K. Kremer, E. Thrane, and P. D. Lasky, *Astrophys. J. Lett.* **921**, L43 (2021), [arXiv:2106.09042 \[astro-ph.HE\]](#).
 - [42] C. Konigsdorffer and A. Gopakumar, *Phys. Rev. D* **73**, 124012 (2006), [arXiv:gr-qc/0603056 \[gr-qc\]](#).
 - [43] N. Yunes, K. G. Arun, E. Berti, and C. M. Will, *Phys. Rev. D* **80**, 084001 (2009), [Erratum: *Phys. Rev. D* **89**, 109901 (2014)], [arXiv:0906.0313 \[gr-qc\]](#).
 - [44] A. Klein and P. Jetzer, *Phys. Rev. D* **81**, 124001 (2010), [arXiv:1005.2046 \[gr-qc\]](#).
 - [45] C. K. Mishra, K. G. Arun, and B. R. Iyer, *Phys. Rev. D* **91**, 084040 (2015), [arXiv:1501.07096 \[gr-qc\]](#).
 - [46] B. Moore, M. Favata, K. G. Arun, and C. K. Mishra, *Phys. Rev. D* **93**, 124061 (2016), [arXiv:1605.00304 \[gr-qc\]](#).
 - [47] S. Tanay, M. Haney, and A. Gopakumar, *Phys. Rev. D* **93**, 064031 (2016), [arXiv:1602.03081 \[gr-qc\]](#).
 - [48] A. Klein, Y. Boetzel, A. Gopakumar, P. Jetzer, and L. de Vittori, *Phys. Rev. D* **98**, 104043 (2018), [arXiv:1801.08542 \[gr-qc\]](#).
 - [49] Y. Boetzel, C. K. Mishra, G. Faye, A. Gopakumar, and B. R. Iyer, *Phys. Rev. D* **100**, 044018 (2019), [arXiv:1904.11814 \[gr-qc\]](#).
 - [50] M. Ebersold, Y. Boetzel, G. Faye, C. K. Mishra, B. R. Iyer, and P. Jetzer, *Phys. Rev. D* **100**, 084043 (2019), [arXiv:1906.06263 \[gr-qc\]](#).
 - [51] B. Moore and N. Yunes, *Class. Quant. Grav.* **36**, 185003 (2019), [arXiv:1903.05203 \[gr-qc\]](#).
 - [52] A. Klein, (2021), [arXiv:2106.10291 \[gr-qc\]](#).
 - [53] M. Khalil, A. Buonanno, J. Steinhoff, and J. Vines, *Phys. Rev. D* **104**, 024046 (2021), [arXiv:2104.11705 \[gr-qc\]](#).
 - [54] K. Paul and C. K. Mishra, *Phys. Rev. D* **108**, 024023 (2023), [arXiv:2211.04155 \[gr-qc\]](#).
 - [55] Q. Henry and M. Khalil, *Phys. Rev. D* **108**, 104016 (2023), [arXiv:2308.13606 \[gr-qc\]](#).
 - [56] I. Hinder, L. E. Kidder, and H. P. Pfeiffer, *Phys. Rev. D* **98**, 044015 (2018), [arXiv:1709.02007 \[gr-qc\]](#).
 - [57] E. A. Huerta *et al.*, *Phys. Rev. D* **97**, 024031 (2018), [arXiv:1711.06276 \[gr-qc\]](#).
 - [58] Z. Cao and W.-B. Han, *Phys. Rev. D* **96**, 044028 (2017), [arXiv:1708.00166 \[gr-qc\]](#).
 - [59] D. Chiamello and A. Nagar, *Phys. Rev. D* **101**, 101501 (2020), [arXiv:2001.11736 \[gr-qc\]](#).
 - [60] T. Islam, V. Varma, J. Lodman, S. E. Field, G. Khanna, M. A. Scheel, H. P. Pfeiffer, D. Gerosa, and L. E. Kidder, *Phys. Rev. D* **103**, 064022 (2021), [arXiv:2101.11798 \[gr-qc\]](#).
 - [61] A. Chattaraj, T. RoyChowdhury, Divyajyoti, C. K. Mishra, and A. Gupta, *Phys. Rev. D* **106**, 124008 (2022), [arXiv:2204.02377 \[gr-qc\]](#).
 - [62] A. Ramos-Buades, A. Buonanno, M. Khalil, and S. Ossokine, *Phys. Rev. D* **105**, 044035 (2022), [arXiv:2112.06952 \[gr-qc\]](#).
 - [63] X. Liu, Z. Cao, and L. Shao, *International Journal of Modern Physics D* **32**, 2350015 (2023), [arXiv:2306.15277 \[gr-qc\]](#).
 - [64] A. Ramos-Buades, A. Buonanno, and J. Gair, *Phys. Rev. D* **108**, 124063 (2023), [arXiv:2309.15528 \[gr-qc\]](#).
 - [65] K. Paul, A. Maurya, Q. Henry, K. Sharma, P. Satheesh, Divyajyoti, P. Kumar, and C. K. Mishra, (2024), [arXiv:2409.13866 \[gr-qc\]](#).
 - [66] X. Liu, Z. Cao, and L. Shao, *Phys. Rev. D* **101**, 044049 (2020), [arXiv:1910.00784 \[gr-qc\]](#).
 - [67] T. Hinderer and S. Babak, *Phys. Rev. D* **96**, 104048 (2017), [arXiv:1707.08426 \[gr-qc\]](#).
 - [68] S. Albanesi, A. Placidi, A. Nagar, M. Orselli, and S. Bernuzzi, *Phys. Rev. D* **105**, L121503 (2022), [arXiv:2203.16286 \[gr-qc\]](#).
 - [69] A. Nagar, A. Bonino, and P. Rettengo, *Phys. Rev. D* **103**, 104021 (2021), [arXiv:2101.08624 \[gr-qc\]](#).
 - [70] X. Liu, Z. Cao, and Z.-H. Zhu, *Class. Quant. Grav.* **39**, 035009 (2022), [arXiv:2102.08614 \[gr-qc\]](#).
 - [71] Q. Yun, W.-B. Han, X. Zhong, and C. A. Benavides-Gallego, *Phys. Rev. D* **103**, 124053 (2021), [arXiv:2104.03789 \[gr-qc\]](#).
 - [72] E. O’Shea and P. Kumar, *Phys. Rev. D* **108**, 104018 (2023), [arXiv:2107.07981 \[astro-ph.HE\]](#).
 - [73] I. M. Romero-Shaw, P. D. Lasky, and E. Thrane, *Mon. Not. Roy. Astron. Soc.* **490**, 5210 (2019), [arXiv:1909.05466 \[astro-ph.HE\]](#).
 - [74] R. J. E. Smith, G. Ashton, A. Vajpeyi, and C. Talbot, *MNRAS* **498**, 4492 (2020), [arXiv:1909.11873 \[gr-qc\]](#).
 - [75] I. M. Romero-Shaw, P. D. Lasky, and E. Thrane, *Astrophys. J.* **940**, 171 (2022), [arXiv:2206.14695 \[astro-ph.HE\]](#).
 - [76] A. K. Lenon, A. H. Nitz, and D. A. Brown, *MNRAS* **497**, 1966 (2020), [arXiv:2005.14146 \[astro-ph.HE\]](#).
 - [77] I. M. Romero-Shaw, P. D. Lasky, and E. Thrane, *Astrophys. J. Lett.* **921**, L31 (2021), [arXiv:2108.01284 \[astro-ph.HE\]](#).
 - [78] I. M. Romero-Shaw, D. Gerosa, and N. Loutrel, *Mon. Not. Roy. Astron. Soc.* **519**, 5352 (2023), [arXiv:2211.07528 \[astro-ph.HE\]](#).
 - [79] R. Gamba, M. Breschi, G. Carullo, S. Albanesi, P. Rettengo, S. Bernuzzi, and A. Nagar, *Nature Astron.* **7**, 11 (2023), [arXiv:2106.05575 \[gr-qc\]](#).
 - [80] A. Bonino, R. Gamba, P. Schmidt, A. Nagar, G. Pratten, M. Breschi, P. Rettengo, and S. Bernuzzi, *Phys. Rev. D* **107**, 064024 (2023), [arXiv:2207.10474 \[gr-qc\]](#).

- [81] I. M. Romero-Shaw, N. Farrow, S. Stevenson, E. Thrane, and X.-J. Zhu, *MNRAS* **496**, L64 (2020), [arXiv:2001.06492 \[astro-ph.HE\]](#).
- [82] Divyajyoti, S. Kumar, S. Tibrewal, I. M. Romero-Shaw, and C. K. Mishra, *Phys. Rev. D* **109**, 043037 (2024), [arXiv:2309.16638 \[gr-qc\]](#).
- [83] M. Favata, *Phys. Rev. Lett.* **112**, 101101 (2014), [arXiv:1310.8288 \[gr-qc\]](#).
- [84] B. P. Abbott *et al.* (LIGO Scientific, Virgo), *Class. Quant. Grav.* **34**, 104002 (2017), [arXiv:1611.07531 \[gr-qc\]](#).
- [85] M. Favata, C. Kim, K. G. Arun, J. Kim, and H. W. Lee, *Phys. Rev. D* **105**, 023003 (2022), [arXiv:2108.05861 \[gr-qc\]](#).
- [86] A. Ramos-Buades, S. Husa, G. Pratten, H. Estellés, C. García-Quirós, M. Mateu-Lucena, M. Colleoni, and R. Jaume, *Phys. Rev. D* **101**, 083015 (2020), [arXiv:1909.11011 \[gr-qc\]](#).
- [87] P. Narayan, N. K. Johnson-McDaniel, and A. Gupta, *Phys. Rev. D* **108**, 064003 (2023), [arXiv:2306.04068 \[gr-qc\]](#).
- [88] W. Guo, D. Williams, I. S. Heng, H. Gabbard, Y.-B. Bae, G. Kang, and Z.-H. Zhu, *Mon. Not. Roy. Astron. Soc.* **516**, 3847 (2022), [arXiv:2203.06969 \[gr-qc\]](#).
- [89] P. Saini, M. Favata, and K. G. Arun, *Phys. Rev. D* **106**, 084031 (2022), [arXiv:2203.04634 \[gr-qc\]](#).
- [90] S. A. Bhat, P. Saini, M. Favata, and K. G. Arun, *Phys. Rev. D* **107**, 024009 (2023), [arXiv:2207.13761 \[gr-qc\]](#).
- [91] H. Gil Choi, T. Yang, and H. M. Lee, (2022), [arXiv:2210.09541 \[gr-qc\]](#).
- [92] S. Klimentenko, S. Mohanty, M. Rakhmanov, and G. Mitselmakher, *Phys. Rev. D* **72**, 122002 (2005), [arXiv:gr-qc/0508068](#).
- [93] F. Salemi, E. Milotti, G. A. Prodi, G. Vedovato, C. Lazzaro, S. Tiwari, S. Vinciguerra, M. Drago, and S. Klimentenko, *Phys. Rev. D* **100**, 042003 (2019), [arXiv:1905.09260 \[gr-qc\]](#).
- [94] V. Tiwari *et al.*, *Phys. Rev. D* **93**, 043007 (2016), [arXiv:1511.09240 \[gr-qc\]](#).
- [95] S. Roy, *Phys. Rev. Res.* **4**, 033078 (2022), [arXiv:2201.01526 \[gr-qc\]](#).
- [96] B. P. Abbott *et al.* (LIGO Scientific, Virgo), *Astrophys. J.* **883**, 149 (2019), [arXiv:1907.09384 \[astro-ph.HE\]](#).
- [97] B. Abbott *et al.* (LIGO Scientific, Virgo), *Phys. Rev. Lett.* **116**, 061102 (2016), [arXiv:1602.03837 \[gr-qc\]](#).
- [98] S. Klimentenko, I. Yakushin, A. Mercer, and G. Mitselmakher, *Class. Quant. Grav.* **25**, 114029 (2008).
- [99] S. Klimentenko *et al.*, *Phys. Rev. D* **93**, 042004 (2016), [arXiv:1511.05999 \[gr-qc\]](#).
- [100] N. J. Cornish and T. B. Littenberg, *Classical and Quantum Gravity* **32**, 135012 (2015).
- [101] N. J. Cornish, T. B. Littenberg, B. Bécsy, K. Chatziioannou, J. A. Clark, S. Ghonge, and M. Millhouse, *Phys. Rev. D* **103**, 044006 (2021).
- [102] B. Abbott *et al.* (LIGO Scientific, Virgo), *Phys. Rev. X* **9**, 031040 (2019), [arXiv:1811.12907 \[astro-ph.HE\]](#).
- [103] R. Abbott *et al.* (LIGO Scientific, Virgo), *Phys. Rev. X* **11**, 021053 (2021), [arXiv:2010.14527 \[gr-qc\]](#).
- [104] R. Abbott *et al.* (LIGO Scientific, VIRGO), *Phys. Rev. D* **109**, 022001 (2024), [arXiv:2108.01045 \[gr-qc\]](#).
- [105] R. Abbott *et al.* (KAGRA, VIRGO, LIGO Scientific), *Phys. Rev. X* **13**, 041039 (2023), [arXiv:2111.03606 \[gr-qc\]](#).
- [106] R. Abbott *et al.* (LIGO Scientific, Virgo), *Phys. Rev. Lett.* **125**, 101102 (2020), [arXiv:2009.01075 \[gr-qc\]](#).
- [107] M. Szczepańczyk *et al.*, *Phys. Rev. D* **103**, 082002 (2021), [arXiv:2009.11336 \[astro-ph.HE\]](#).
- [108] A. H. Nitz, T. Dal Canton, D. Davis, and S. Reyes, *Phys. Rev. D* **98**, 024050 (2018), [arXiv:1805.11174 \[gr-qc\]](#).
- [109] G. Caneva Santoro, S. Roy, R. Vicente, M. Haney, O. J. Piccinni, W. Del Pozzo, and M. Martinez, *Phys. Rev. Lett.* **132**, 251401 (2024), [arXiv:2309.05061 \[gr-qc\]](#).
- [110] S. H. W. Leong, J. Calderón Bustillo, M. Gracia-Linares, and P. Laguna, *Phys. Rev. D* **108**, 124079 (2023), [arXiv:2308.03250 \[gr-qc\]](#).
- [111] T. Evstafyeva, U. Sperhake, I. M. Romero-Shaw, and M. Agathos, *Phys. Rev. Lett.* **133**, 131401 (2024), [arXiv:2406.02715 \[gr-qc\]](#).
- [112] J. Calderon Bustillo, N. Sanchis-Gual, S. H. W. Leong, K. Chandra, A. Torres-Forne, J. A. Font, C. Herdeiro, E. Radu, I. C. F. Wong, and T. G. F. Li, *Phys. Rev. D* **108**, 123020 (2023), [arXiv:2206.02551 \[gr-qc\]](#).
- [113] V. Varma and P. Ajith, *Phys. Rev. D* **96**, 124024 (2017), [arXiv:1612.05608 \[gr-qc\]](#).
- [114] C. Königsdörffer and A. Gopakumar, *Phys. Rev. D* **73**, 124012 (2006), [arXiv:gr-qc/0603056 \[gr-qc\]](#).
- [115] T. Damour and N. Deruelle, *Annales de l'I.H.P. Physique théorique* **43**, 107 (1985).
- [116] R.-M. Memmesheimer, A. Gopakumar, and G. Schafer, *Phys. Rev. D* **70**, 104011 (2004), [arXiv:gr-qc/0407049 \[gr-qc\]](#).
- [117] K. Arun, A. Buonanno, G. Faye, and E. Ochsner, *Phys. Rev. D* **79**, 104023 (2009), [Erratum: *Phys. Rev. D* **84**, 049901 (2011)], [arXiv:0810.5336 \[gr-qc\]](#).
- [118] S. Ossokine, L. E. Kidder, and H. P. Pfeiffer, *Physical Review D* **88** (2013), [10.1103/physrevd.88.084031](#).
- [119] M. Boyle *et al.*, *Class. Quant. Grav.* **36**, 195006 (2019), [arXiv:1904.04831 \[gr-qc\]](#).
- [120] G. Pratten, S. Husa, C. Garcia-Quirós, M. Colleoni, A. Ramos-Buades, H. Estelles, and R. Jaume, *Phys. Rev. D* **102**, 064001 (2020), [arXiv:2001.11412 \[gr-qc\]](#).
- [121] C. M. Biwer, C. D. Capano, S. De, M. Cabero, D. A. Brown, A. H. Nitz, and V. Raymond, *Publ. Astron. Soc. Pac.* **131**, 024503 (2019), [arXiv:1807.10312 \[astro-ph.IM\]](#).
- [122] LIGO Scientific Collaboration, “LIGO Algorithm Library - LALSuite,” free software (GPL) (2018).
- [123] J. Skilling, in *Bayesian Inference and Maximum Entropy Methods in Science and Engineering: 24th International Workshop on Bayesian Inference and Maximum Entropy Methods in Science and Engineering*, American Institute of Physics Conference Series, Vol. 735, edited by R. Fischer, R. Preuss, and U. V. Tossaint (2004) pp. 395–405.
- [124] J. S. Speagle, *Monthly Notices of the Royal Astronomical Society* **493**, 3132 (2020).
- [125] G. Ashton *et al.*, *Astrophys. J. Suppl.* **241**, 27 (2019), [arXiv:1811.02042 \[astro-ph.IM\]](#).
- [126] I. M. Romero-Shaw *et al.*, *Mon. Not. Roy. Astron. Soc.* **499**, 3295 (2020), [arXiv:2006.00714 \[astro-ph.IM\]](#).
- [127] PyCBC, “aLIGOZeroDetHighPower function used for adv ligo psd,” <https://pycbc.org/pycbc/latest/html/pycbc.psd.html> (2018).
- [128] PyCBC, “AdvVirgo function used for virgo psd,” <https://pycbc.org/pycbc/latest/html/pycbc.psd.html> (2012).

- [129] A. Nitz, I. Harry, D. Brown, *et al.*, “[gwastro/pycbc: Pycbc release v1.16.11](#),” (2020).
- [130] C. R. Harris, K. J. Millman, S. J. van der Walt, *et al.*, [Nature](#) **585**, 357 (2020), [arXiv:2006.10256 \[cs.MS\]](#).
- [131] C. Hoy and V. Raymond, [SoftwareX](#) **15**, 100765 (2021), [arXiv:2006.06639 \[astro-ph.IM\]](#).
- [132] J. D. Hunter, [Computing in Science and Engineering](#) **9**, 90 (2007).
- [133] M. L. Waskom, [Journal of Open Source Software](#) **6**, 3021 (2021).
- [134] T. Kluyver, B. Ragan-Kelley, F. Pérez, *et al.*, in *Positioning and Power in Academic Publishing: Players, Agents and Agendas*, edited by F. Loizides and B. Schmidt (IOS Press, 2016) pp. 87–90.